Gravitational waves from the Papaloizou-Pringle instability in black hole-torus systems

Kenta Kiuchi,[1] Masaru Shibata,[1] Pedro J. Montero,[2] and José A. Font[3]

[1] *Yukawa Institute for Theoretical Physics, Kyoto University, Kyoto, 606-8502, Japan*
[2] *Max-Planck-Institute für Astrophysik, Karl-Schwarzschild-Str. 1, 81748, Garching bei München, Germany*
[3] *Departamento de Astronomía y Astrofísica, Universitat de València, Dr. Moliner 50, 46100 Burjassot, Spain*

(Dated: May 26, 2011)

Black hole (BH)–torus systems are promising candidates for the central engine of gamma-ray bursts (GRBs), and also possible outcomes of the collapse of supermassive stars to supermassive black holes (SMBHs). By three-dimensional general relativistic numerical simulations, we show that an $m = 1$ nonaxisymmetric instability grows for a wide range of self-gravitating tori orbiting BHs. The resulting nonaxisymmetric structure persists for a timescale much longer than the dynamical one, becoming a strong emitter of large amplitude, quasiperiodic gravitational waves. Our results indicate that both, the central engine of GRBs and newly formed SMBHs, can be strong gravitational wave sources observable by forthcoming ground-based and spacecraft detectors.

PACS numbers: 04.25.D-, 04.30.-w, 04.40.Dg

arXiv:1105.5035v1 [astro-ph.HE] 25 May 2011

Introduction.— Black hole (BH)–torus systems are common in the universe. The central region of active galactic nuclei is believed to consist of a supermassive black hole (SMBH) of mass $M_{\rm BH} \sim 10^6$–$10^{10} M_\odot$ surrounded by a torus. Such systems may form through the collapse of supermassive stars (SMS) [1, 2]. Mergers of neutron star (NS) binaries and BH-NS binaries often result in a BH and a torus [3]. Such systems can also be produced at the end of the life of massive stars [4]. It has been suggested that the merger and collapsar scenarios are linked to short- and long-duration gamma-ray bursts (GRBs), respectively [5, 6]. Thus, BH-torus systems may become high-energy astrophysical objects. However, their formation and evolution have not yet been observed as such sites are opaque to electromagnetic waves (EWs) due to their intrinsic high density and temperature. Gravitational waves (GWs), however, are much more transparent than EWs with respect to absorption and scattering with matter. If BH–torus systems emitted detectable GWs, it would be possible to explore their formation and evolution, along with the prevailing hypotheses that associate them to GRB engines. This may become possible in the near future thanks to the array of ground-based (LIGO, VIRGO, LCGT) and spacecraft (LISA) detectors of GWs [7].

BH-torus systems are known to be subject to the axisymmetric runaway instability [8], and the nonaxisymmetric Papaloizou-Pringle instability (PPI) [9]. Recently, general relativistic (GR) simulations have shown that the runaway instability does not have a significant impact on the dynamics even if the torus self-gravity is taken into account [10]. However, nonaxisymmetric features may still play a crucial role as shown by linear analysis [11]. Exploring the nonlinear growth and saturation of the PPI in BH–torus systems requires three-dimensional (3D) simulations [12]. Moreover, since GR plays an important role in the case of self-gravitating tori [13], 3D GR numerical simulations are mandatory. In particular, long-term simulations are essential to follow the BH–torus systems after the PPI saturation. By contrast, the recent 3D GR simulations of BH–torus by Korobkin et al. only followed the linear growth phase of the PPI [13].

In this *Letter* we report results of a sample of such simulations which show that the PPI sets in for a wide range of BH–torus systems, and that the resulting nonaxisymmetric structure is maintained after the saturation of the instability. As a result, such systems can be strong sources of detectable GWs for the detectors that will be in operation in the near future. We use units of $c = G = 1$, and the perturbation is expressed by the expansion of $\exp\{-i(\omega t - m\varphi)\}$.

Method and initial models.— The simulations are performed using a fixed mesh refinement (FMR) and Message Passing Interface version of the SACRA code (see [14] for details regarding the implementation of the FMR algorithm and the formulation and numerical schemes for solving Einstein's and hydrodynamics equations). The FMR structure consists of 6 refinement levels for which the grid resolution changes as $\Delta x_{l-1} = 2\Delta x_l$ (l = 2–6), with a finest level of $\Delta x_{l=6} = 0.05 M_{\rm BH}$. Each domain is composed of $(2N+1, 2N+1, N+1)$ Cartesian grid zones (x, y, z) which cover the interval $[-N\Delta x_l : N\Delta x_l]$ for the $x-$ and $y-$directions and $[0 : N\Delta x_l]$ along z, with $N = 98$. The outer boundary is located at $156.8 M_{\rm BH}$ which is in the local wave zone (see Table I). The BH horizon is covered by ≈ 10 grid points in the finest refinement level. For assessing the validity of the numerical results, simulations with different values of $\Delta x_{l=6}$, N, and size of each domain were performed, which confirmed that convergence is achieved with our chosen values. We use a standard Γ-law equation of state (EOS) $P = (\Gamma - 1)\rho\varepsilon$, where P is the pressure, ρ the rest-mass density, ε the specific internal energy, and Γ the adiabatic index.

TABLE I: List of key quantities for the initial data: specific angular momentum profile (value of $j/M_{\rm BH}$ at the inner edge), torus-to-BH mass ratio, $\mathcal{R} \equiv M_{\rm tor}/M_{\rm BH}$, position of the inner edge, center (location of the maximum density), and outer edge on the equatorial plane, $r_{\rm in}$, $r_{\rm c}$, and $r_{\rm out}$, orbital period at $r = r_{\rm c}$, $t_{\rm orb}$, and simulation time in units of $t_{\rm orb}$. The last two columns show the growth rate $\mathrm{Im}(\omega_m)$ of the PPI and the Fourier amplitude of the density perturbation for the $m = 1$ mode at the saturation, $\delta_1 \equiv |D_1|/D_0$. Here, $\Omega_{\rm c}$ is the angular velocity at $r = r_{\rm c}$.

Model	j profile	$M_{\rm tor}/M_{\rm BH}$	$r_{\rm in}/M_{\rm BH}$	$r_{\rm c}/M_{\rm BH}$	$r_{\rm out}/M_{\rm BH}$	$t_{\rm orb}/M_{\rm BH}$	$t_{\rm sim}/t_{\rm orb}$	$\mathrm{Im}(\omega_1)/\Omega_{\rm c}$	δ_1
C1	constant (3.83)	0.10	3.3	8.02	19.8	172.6	≈ 34	0.142	≈ 0.1
C06	constant (3.80)	0.06	3.6	8.01	19.8	171.6	≈ 40	0.089	≈ 0.1
NC1	$j \propto r^{0.26}$(3.53)	0.10	4.8	10.9	19.8	257.9	≈ 36	0.056	≈ 0.25
NC06	$j \propto r^{0.29}$(3.62)	0.06	5.0	11.7	20.0	284.0	≈ 34	—	—

Compact equilibria for a BH–torus system are prepared in the puncture framework and used as initial conditions [15]. We adopt the $\Gamma = 4/3$ polytropic EOS, $P = \kappa\rho^{\Gamma}$, to mimic the EOS of a degenerate relativistic electron gas or radiation dominated gas. The polytropic constant κ is chosen such that the torus-to-BH mass ratios are in the range $\mathcal{R} = M_{\rm tor}/M_{\rm BH} = 0.06$–$0.1$. We specify the angular momentum profiles, $j = j(\Omega)$, where $j \equiv (1+\varepsilon+P/\rho)u_\varphi$ and $\Omega = u^\varphi/u^t$, u^μ denoting the fluid four velocity. Table I lists key quantities of the four different BH-torus systems considered. The BH is assumed to be non-rotating. We investigate both j =constant (C models), and non-constant profiles (NC models) with $j \propto \Omega^{-1/6}$, to assess their influence. The selected mass ratios are partially motivated by the result of simulations of gravitational collapse to a BH and torus [2, 16]. The numerical model of [16] may be regarded as a candidate of the central engine of GRBs, and that of [2] as a model for the formation of a SMBH through the collapse of a rotating SMS.

Our numerical simulations are performed for a time long enough, i.e. $t \sim 20$–$40\ t_{\rm orb}$, to include the growth, saturation, and post-saturation phases of the PPI, for which the growth timescale is of order $t_{\rm orb}$ (see Table I).

Results.— Figure 1 shows the evolution of the maximum baryon rest-mass density of the torus, the baryon rest-mass flux measured on the apparent horizon (AH), $\dot{M}_{\rm r=r_{AH}}$, and the total baryon rest-mass located outside the AH for each model. Figure 2 shows snapshots of the rest-mass density distribution on the equatorial plane after the PPI saturation for models C1 and NC1. Figure 3 shows the time evolution of the density perturbation amplitudes for the $m = 1$–3 modes of model C1, a typical power-law index of the angular velocity, and the outgoing component of the complex Weyl scalar $\Psi_4^{(2,2)}$ with $l = m = 2$ mode for models C1 and NC1, where $t_{\rm ret}$ is the retarded time.

These figures reveal that the PPI is present in all models except NC06. The instability grows exponentially with time, with the $m = 1$ mode being the fastest growing mode (cf. Fig. 3(a)). Figure 1(a) indicates that during the linear growth phase, the maximum density is approximately constant, but after several orbits, nonlinear growth sets in and $\rho_{\rm max}$ increases. After saturation, $\rho_{\rm max}$ decreases and eventually approaches a new quasiequilibrium value. For a given angular momentum profile, the PPI growth timescale is shorter the larger the mass ratio $\mathcal{R}$. For a given mass ratio, the growth timescale for NC models is longer than for C models.

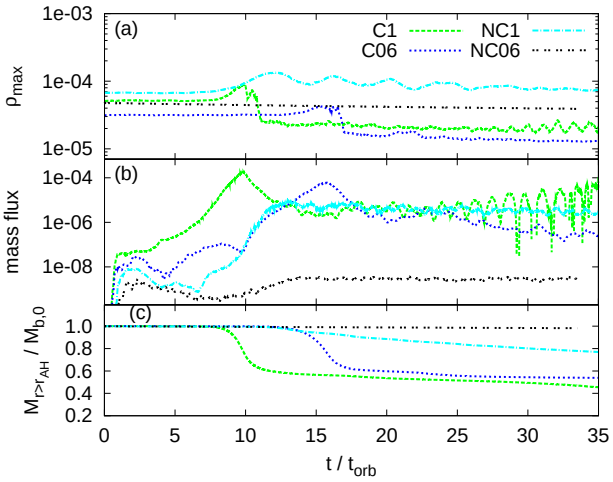

FIG. 1: Evolution of (a) the maximum rest-mass density, (b) the mass flux on the BH horizon, and (c) the rest-mass located outside the apparent horizon (AH) for each model. The maximum density is evaluated outside the AH and rest-mass is normalized by its initial value.

As shown in Fig. 1(b), the mass flux increases exponentially with the PPI growth. It reaches its peak value at mode growth saturation and then settles to an approximately non-zero constant value. These features are qualitatively identical for the PPI unstable models. The mass flux for NC06 is negligible throughout the evolution. These features are reflected in Fig. 1(c): Around the saturation time of the PPI nonlinear growth, the torus mass steeply decreases, and then the torus relaxes to a stationary accretion state. For NC models, the mass flux at the saturation time is always lower than for C models, which indicates the dependence of the accretion history on the profile of j. In Fig. 2 we illustrate the nonaxisymmetric morphological features present in the tori of models C1

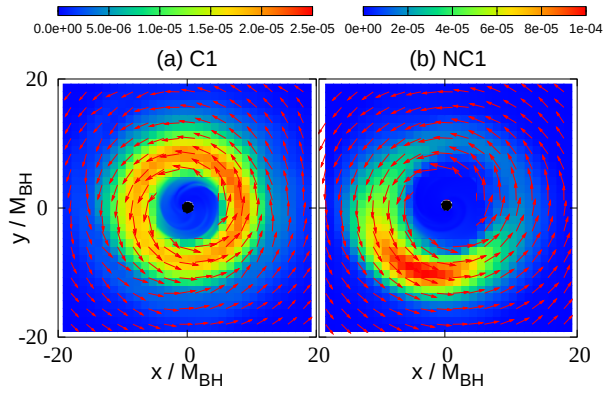

FIG. 2: Snapshots of the rest-mass density distribution on the equatorial plane for models C1 at $t = 15.11\ t_{\rm orb}$ (left) and NC1 at $t = 20.02\ t_{\rm orb}$ (right). Vectors show the velocity fields, and black filled circles around the centers show the region inside the AHs.

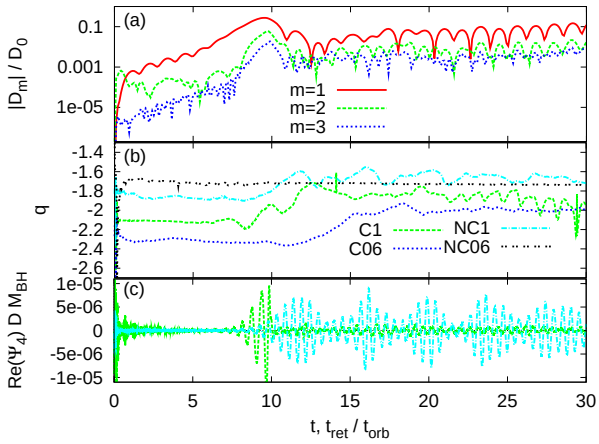

FIG. 3: Evolution of (a) the $m = 1$–3 mode amplitudes for model C1, (b) the power–law index of the angular velocity profile for all models, and (c) the outgoing part of the complex Weyl scalar $\mathrm{Re}(\Psi_4^{(2,2)})$ for models C1 (green) and NC1 (blue).

and NC1 once the stationary accretion phase is reached. The presence of the $m = 1$ mode is apparent. These results imply that more massive tori and/or a $j =$ const profile favor the appearance of the PPI with respect to less massive tori and/or a $j \neq$ const profile, for which the torus may be PP-stable (e.g. model NC06). In addition, no sign of the runaway instability is found for any models.

Figure 3(a) plots the evolution of the Fourier modes for the density perturbation of model C1, for which we define $D_m = \int \rho\, \mathrm{e}^{-im\varphi} d^3x$ and $\delta_m \equiv |D_m|/D_0$. This shows that the $m = 1$ mode is the fastest growing mode and that saturation occurs at $t \sim 10\ t_{\rm orb}$. We determine the PPI growth rate through a fit of the numerical data, and find it in a wide range $\sim$ 5–25% of the angular velocity at the saturation time (see Table I). As expected from Fig. 1, massive and/or $j =$ const models exhibit larger growth rates (in agreement with [13]) and no evidence of the instability is found for model NC06.

The PPI activates the transport of angular momentum outwards through the corotation point resonance [11], and therefore, redistributes angular momentum. Figure 3(b) shows the evolution of a typical power-law index of the angular velocity profile, where we fit $\bar{\Omega}(r) \equiv 1/2\pi \int \Omega(r, \pi/2, \varphi)\, d\varphi$ by $\propto r^q$ for $r \in [r_{\rm in}, r_{\rm out}]$ on the equatorial plane. In Newtonian gravity $q = -2$ for $j =$ const and $q = -1.5$ for Keplerian motion. It is expected that q would approach -1.5 (Keplerian limit) from a lower initial value < -1.5. Note that in GR $j =$ const law does not correspond to $q = -2$ and also $q \neq -1.5$ for the Keplerian limit. Figure 3(b) shows that after the onset of the PPI (for all models except for NC06), q increases and then saturates, reflecting the outward transport of angular momentum. The increase of q indicates that tori with a positive value of dj/dr are stable against the PPI, as expected from linear analysis [11] and from previous nonlinear simulations [12]. All the features found here suggest that the PPI plays an important role for the BH-torus system dynamics unless the torus mass is small and the angular momentum profile is close to the Keplerian profile.

A point worth stressing is that the $m = 1$ nonaxisymmetric structure survives with an appreciable amplitude after the saturation of the PPI nonlinear growth, as shown in Fig. 2. The likely reason is that as the common center of mass for the BH–torus system should remain at the origin and the BH center is not located at the center of mass, then the torus should be deformed. The persistent $m = 1$ structure leads to the emission of quasiperiodic GWs with a large amplitude. Note that the dominant mode of GWs is $l = m = 2$ because the situation is similar to a test particle orbiting around a BH. An outgoing component of the Weyl scalar extracted in the local wave zone, plotted in Fig. 3(c) for model C1 (green curve), shows that the waveforms reflect the evolution of the system: A burst at $t_{\rm ret}/t_{\rm orb} \approx 10$ is emitted by the PPI nonlinear growth and saturation, and subsequent quasiperiodic waves for $t_{\rm ret}/t_{\rm orb} \gtrsim 10$ are emitted by the long-lived $m = 1$ structure. This feature is universal for all the C models. While the GW for the NC1 model (Fig. 3(c), blue curve) does not show a prominent burst, they do show the quasiperiodic emission induced by the long-lived $m = 1$ structure. The striking modulation in the GW signal found only in $j \neq$ const models may be due to the variability in the maximum rest-mass density and the q-index for the angular velocity after mode growth saturation (between $10t_{\rm orb} < t < 30t_{\rm orb}$ for model NC1). Therefore, it may be associated with the excitation of p-modes (pressure-inertial modes) in the torus. These p-mode oscillations are gradually damped, as well as the modulation, for $t > 30t_{\rm orb}$. The emission of quasiperiodic GWs is expected to continue as far as the disk has a significant amount of mass. Such time duration can be

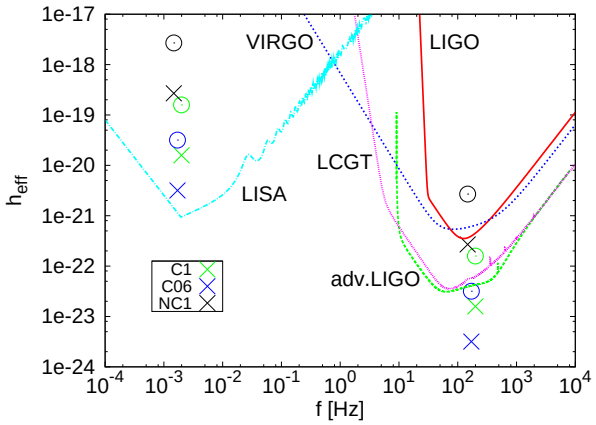

FIG. 4: GW spectra for all the models for $M_{\rm BH} = 10M_\odot$ and $D = 100$ Mpc, and $M_{\rm BH} = 10^6 M_\odot$ and $D = 10$ Gpc. The cross symbols show the peak amplitudes found in the numerical simulations and the circles show hypothetical amplitudes inferred from accretion timescales (see main text for details).

estimated from the mass accretion rate, and the residual disk mass (Fig. 1(b) and (c)). We find the accretion timescales are $t_{\rm acc} \sim M_{\rm r>r_{AH}}/\dot{M}_{\rm r=r_{AH}} \approx 1$–$8 \times 10^4\ M_{\rm BH}$.

In Fig. 4 we show with crosses the peak effective amplitude $h_{\rm eff}$ of GWs together with the design sensitivities of ground-based and spacecraft GW detectors [7]. Here $h_{\rm eff} = (\{|\tilde{h}_+|^2 + |\tilde{h}_\times|^2\}/2)^{1/2} D/M_{\rm BH}$ with $\tilde{h}_{+,\times}$ and D being the Fourier component of two polarization modes and the distance from the source. Since our focus is on the GW emission after the PPI growth saturation, we discard the waveform before the saturation for the C models, e.g. for $t_{\rm ret}/t_{\rm orb} \lesssim 10$ for C1, when calculating $h_{\rm eff}$. From the accretion timescale $t_{\rm acc}$, we may expect that the GW emission will continue for $N_{\rm cycle} \sim t_{\rm acc}/t_{\rm GW} \approx 100$ where $t_{\rm GW}$ is the typical oscillation period of GWs. Hence, the peak amplitudes may be enhanced by $\sqrt{N_{\rm cycle}} \sim 10$, values plotted with circles in Fig. 4. Because we use units of $M_{\rm BH} = 1$ in our simulations, the numerical results can be rescaled for arbitrary BH mass. We choose the hypothetical values for the collapsar model of GRB central engine as $(M_{\rm BH}, D) = (10M_\odot, 100\ {\rm Mpc})$ and for the hypothetical formation scenario of a SMBH through SMS collapse as $(M_{\rm BH}, D) = (10^6 M_\odot, 10\ {\rm Gpc})$ in Fig. 4.

For the stellar-mass BH, $h_{\rm eff}$ could be $\sim 10^{-21}$ at the peak with the frequency 100–200 Hz, which corresponds to the Kepler frequency of $r_{\rm orb} \approx 10M_{\rm BH}$. The peak amplitudes agree with the order estimation,

$$h_{\rm peak} \sim \frac{2M_{m=1}v^2}{D}\sqrt{N_{\rm cycle}}$$
$$\approx 3\times 10^{-21}\left(\frac{\delta_1}{0.1}\right)\left(\frac{\mathcal{R}}{0.1}\right)\left(\frac{M_{\rm BH}}{10M_\odot}\right)\left(\frac{100{\rm Mpc}}{D}\right)\left(\frac{N_{\rm cycle}}{100}\right)^{1/2},$$

where $M_{m=1}$ is the mass of matter which contributes to the $m = 1$ structure (see also Table I) and we assume the Kepler motion with radius $\approx 10M_{\rm BH}$. The amplitude of the enhanced peaks could be larger than the noise level of the advanced ground-based detectors. For the SMBH formation scenario with $(M_{\rm BH}, D) = (10^6 M_\odot, 10\ {\rm Gpc})$, the predicted peak amplitude is $h_{\rm eff} \sim 10^{-18}$–$10^{-19}$ with the frequency $\sim 10^{-3}$ Hz. Such GWs would be detected with a high signal-to-noise ratio $\gtrsim 10$ by LISA.

Summary and discussion.— We have explored the PPI in BH–torus systems in the framework of numerical relativity. We have found that the $m = 1$ PPI occurs for a wide range of self-gravitating tori orbiting BHs. The resulting $m = 1$ structure in the torus survives for a long time after the PPI growth saturation, and large amplitude, quasiperiodic GWs are emitted. For reasonable hypothetical masses and distances, we have found that the quasiperiodic GWs emitted by this mechanism could be a promising source for ground-based and spacecraft detectors (for stellar-mass BHs and SMBHs, respectively).

The BH–torus system composed of a stellar-mass BH is a promising candidate for the central engine of GRBs, and our results suggest that the so-called collapsar hypothesis [6] may be verified via observation of GWs. In GRBs, jets are likely to be ejected along the rotation axis of a spinning BH and torus. If the BH–torus system formed in the collapsar is axially symmetric, GWs of $l = 2$ and $m = 0$ mode are primarily emitted in the direction perpendicular to the rotation axis (e.g. [16]). By contrast, the quasiperiodic GWs studied in this letter are emitted along the rotation axis because the $l = m = 2$ mode is dominant. Therefore, it could be possible to observe GRBs and GWs simultaneously, and to explore the collapsar scenario via GW observation. On the other hand, in the formation of a SMBH following SMS collapse, the torus-to-BH mass ratio is predicted to be 0.05–0.1 [2]. Our results suggest that the PPI could grow in such a system. This implies that this scenario may be confirmed by the GW detector LISA.

Acknowledgments.— KK thanks to Y. Suwa for fruitful comments. Numerical computations were performed on XT4 at CfCA of NAOJ and on NEC-SX8 at YITP of Kyoto University. This work was supported by Grant-in-Aid for Young Scientists (B) 22740178, for Scientific Research (21340051), for Scientific Research on Innovative Area (20105004), by HPCI Strategic Program of Japanese MEXT, by the Deutsche Forschungsgesellschaft (DFG SFB/Transregio 7) and by the Spanish MICINN (AYA 2010-21097-C03-01).

[1] M. J. Rees, Ann. Rev. Astron. Astrophys. **22**, 471 (1984).
[2] M. Shibata and S. L. Shapiro, Astrophys. J. **572**, L39 (2002); S. L. Shapiro and M. Shibata, Astrophys. J. **577**, 904 (2002).
[3] e.g., L. Rezzolla, et al., Class. Quant. Grav. **27**, 114105 (2010); K. Kiuchi, et al., Phys. Rev. Lett. **104**, 141101 (2010); Z.B. Etienne, et al., Phys. Rev. D **79**, 044024

(2009); K. Kyutoku, M. Shibata and K. Taniguchi, Phys. Rev. D **82**, 044049 (2010); F. Foucart et al., Phys. Rev. D **83**, 024005 (2010).
[4] A. Heger, et al., Astrophys. J. **591**, 288 (2003).
[5] R. Narayan, B. Paczynski and T. Piran, Astrophys. J. **395**, L83 (1992).
[6] S. E. Woosley, Astrophys. J. **405**, 273 (1993).
[7] LSC Algorithms Library, http://www.lsc-group.phys.uwm.edu/daswg/projects/lal.html for LIGO, advanced LIGO, and VIRGO: Kuroda, K et al., CQG **27** (2010) 084004 for LCGT: S. L. Larson, W. A. Hiscock and R. W. Hellings, Phys. Rev. D **62**, 062001 (2000) for LISA.
[8] M. A. Abramowicz, M. Calvani, and L. Nobili, Nature, **302**, 597 (1983).
[9] J. C. B. Papaloizou and J. E. Pringle, Mon. Not. Roy. Astron. Soc. **208**, 721 (1984).
[10] P. J. Montero, J. A. Font and M. Shibata, Phys. Rev. Lett. **104**, 191101 (2010).
[11] R. Narayan, P. Goldreich and J. Goodman, Mon. Not. Roy. Astron. Soc. **228**, 1 (1987).
[12] O. M. Blaes and J. F. Hawley, Astrophys. J., **326**, 277 (1988): J. F. Hawley, Astrophys. J., **381**, 496 (1991): J. D. Villiers and J. F. Hawley, Astrophys. J., **577**, 866 (2002).
[13] O. Korobkin, et al., Phys. Rev. D **83**, 043007 (2011).
[14] T. Yamamoto, M. Shibata and K. Taniguchi, Phys. Rev. D **78**, 064054 (2008).
[15] M. Shibata, Phys. Rev. D **76**, 064035 (2007).
[16] Y. Sekiguchi and M. Shibata, arXiv:1009.5303.